Stabilized image reconstruction algorithm for synthetic aperture imaging radiometers

Eric Anterrieu

CERFACS

Global Change & Climate Modelling Team

June 1st, 2003

WN/CMGC/03/42

Stabilized image reconstruction algorithm for synthetic aperture imaging radiometers

Eric Anterrieu

June 1st, 2003

Abstract

Synthetic aperture imaging radiometers (SAIR) are potential powerful instruments for high-resolution observation of planetary surfaces at low microwave frequencies. This working note deals with the reconstruction of radiometric brightness temperature maps from SAIR interferometric measurements. It is demonstrated that the corresponding inverse problem is not well-posed, unless a regularizing constraint is introduced in order to provide a unique and stable solution. A new approach is presented by referring to the notion of modelling operator, and to the concept of resolving matrix of the instrument. To illustrate the theory, numerical simulations are carried out for the SMOS space mission, a project led by the European Space Agency (ESA) and devoted to the remote sensing of Soil Moisture and Ocean Salinity from a low orbit platform. The Y-shaped array selected for SMOS is fitted with equally spaced antennae and leads to natural hexagonal sampling grids. Results obtained for this design are presented and discussed with emphasis on stability and error analysis.

keywords: interferometry, radiometry, aperture synthesis, imaging, inverse problem, regularization.

1 Introduction

The SMOS (Soil Moisture and Ocean Salinity) space mission [1] is currently undergoing phase B studies in the framework of the Earth Explorer Program of the European Space Agency. It will be the first attempt to apply, to remote sensing of the Earth surface from space, the concept of the synthetic aperture imaging radiometers (SAIR) [2], initially developed for radio astronomy [3]. This two-dimensional interferometer operating in the L-band is devoted to the remote sensing of soil moisture and ocean salinity from a low orbit platform. Such measurements are required for the establishing of global climate models involving the hydrological cycle of the Earth as well as the global energy balance [4].

From the general point of view of the remote sensing of planetary surfaces at low microwave frequencies, Synthetic Aperture Imaging Radiometers (SAIR) are potential powerful sensors for high-resolution observations. They overcome some of the technical challenges associated with the deployment of large scanning antennae into space by applying aperture synthesis techniques to radiometric interferometers. This working note reports on a new approach for retrieving the radiometric brightness temperatures from SAIR interferometric measurements. In the case of SMOS, these complex visibilities are obtained from raw data inside a star-shaped domain over an hexagonally sampled grid. Hexagonal processing is therefore here the natural way of performing synthetic aperture imaging [5]. However, the method presented in this report is general and could be applied to any 1D or 2D design providing experimental measurements on regular sampling grids.

The first part of this note is devoted to the modelling of the instrument. The relationships between the measured complex visibilities and the brightness temperature of the scene under observation are recalled, focussing on a real instrument which is affected by non-ideal subsystems. In the second part, periodic lattices are introduced, focussing on hexagonal periodic ones because they are necessary for illustrating the processing of the SMOS interferometric measurements. These periodic lattices are the foundations for introducing the sampling grids, then the working spaces, and finally the operators involved in the reconstruction process. The third part is concerned with the reconstruction of the brightness temperature from measured complex visibilities. It is shown that this inverse problem is ill-posed, and must therefore be regularized in order to provide a unique and stable solution. Since SAIR belong to the family of band-limited imaging devices, the problem is reformulated by taking into account the capabilities of the instrument. A regularized approach is presented by referring to the modelling of the instrument. Finally, to illustrate the theory, this report is completed with numerical simulations for the SMOS case. A thorough examination of the stability of the reconstruction process is made, and the propagation of input errors is analyzed.

2 Instrument modelling

A traditional total-power radiometer maps the brightness temperature over a given field of view by scanning a highly directive antenna, either mechanically or electronically, and measuring the power collected in the main beam direction [6]. On the other hand, as illustrated in Figure 1, interferometer radiometers devoted to Earth observation measure the correlation between the signals collected by two spatially separated non-directive antennae which have overlapping fields of view, yielding samples of the coherence function $V(\mathbf{u})$, also termed complex visibilities [3]. The spatial frequencies $\mathbf{u}$ for which these measurements are performed depend on the geometry of the interferometric array. For example, in the case of SMOS, the array that has been selected is a Y-shaped one fitted with equally spaced antennae [1].

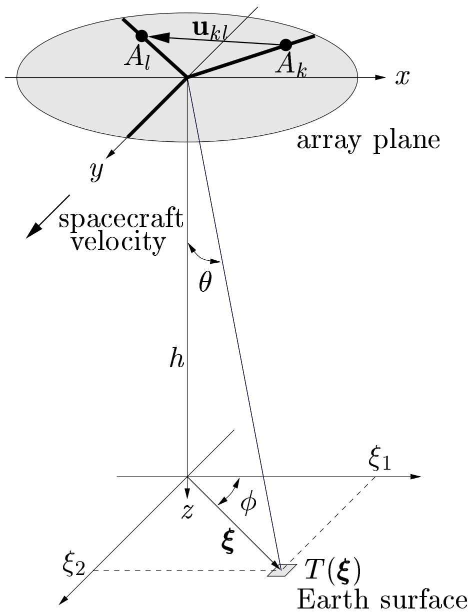

Figure 1: Coordinates systems used when viewing the Earth from an elevation h above the sea surface. The right handed frame (x, y, z) is centred at the origin of the array: z axis is perpendicular to the array plane and points in the viewing direction, y axis is in the array plane and points in the direction of the platform velocity vector, and x axis in the array plane complets this right handed frame. The components ξ_1 and ξ_2 of the angular position variable $\boldsymbol{\xi}$ are direction cosines, θ and ϕ are the traditional spherical coordinates, $\mathbf{u}_{kl}$ is the baseline vector between the two antennae A_k and A_l.

Depending on the modelling of the instrument, integral expressions have been given relating the brightness temperature distribution to the coherence function.

For an ideal interferometer with identical receivers and antennae, and negligible decorrelation effects, the visibility function $V(\mathbf{u})$ and the brightness temperature $T(\boldsymbol{\xi})$ of the scene under observation are related to one another by a Fourier like integral:

$$V(\mathbf{u}_{kl}) \propto \frac{1}{\Omega} \iint_{\|\boldsymbol{\xi}\| \leq 1} |F(\boldsymbol{\xi})|^2 T(\boldsymbol{\xi}) \, \mathrm{e}^{-2\mathrm{j}\pi \mathbf{u}_{kl}\boldsymbol{\xi}} \frac{\mathrm{d}\boldsymbol{\xi}}{\sqrt{1 - \|\boldsymbol{\xi}\|^2}}, \tag{1}$$

where $|F(\boldsymbol{\xi})|^2$ is the power gain pattern of the interferometric antenna elements (here assumed to be identical and with an equivalent solid angle Ω), and $\mathbf{u}_{kl}$ is the spatial frequency associated with the two antennae A_k and A_l (namely, the spacing between the antennae normalized to the central wavelength of observation). The components $\xi_1 =$

$\sin\theta\cos\phi$ and $\xi_2 = \sin\theta\sin\phi$ of the angular position variable $\boldsymbol{\xi}$ are direction cosines, θ and ϕ are the traditional spherical coordinates. Referring back to Figure 1, $-\xi_1$ represents the across track coordinate and ξ_2 the along track coordinate.

However, in a real system, the imperfections of the subsystems of the interferometer affect the measurements of the coherence function samples. As a consequence, in a real interferometer, the relationship between the visibility samples and the brightness temperature distribution differs from the straight Fourier transform expressed by equation (1) and is given by [3][7]:

$$V(\mathbf{u}_{kl}) \propto \frac{1}{\sqrt{\Omega_k\Omega_l}} \iint_{\|\boldsymbol{\xi}\|\leq 1} F_k(\boldsymbol{\xi})\overline{F}_l(\boldsymbol{\xi})T(\boldsymbol{\xi})\widetilde{r}_{kl}\left(\frac{-\mathbf{u}_{kl}\boldsymbol{\xi}}{f_o}\right) \mathrm{e}^{-2\mathrm{j}\pi\mathbf{u}_{kl}\boldsymbol{\xi}} \frac{\mathrm{d}\boldsymbol{\xi}}{\sqrt{1-\|\boldsymbol{\xi}\|^2}}. \tag{2}$$

Here, $F_k(\boldsymbol{\xi})$ and $F_l(\boldsymbol{\xi})$ are the voltage patterns of the two antennae A_k and A_l (the overbar indicates the complex conjugate), Ω_k and Ω_l are the equivalent solid angles of these antennae, $\widetilde{r}_{kl}(t)$ is the so called fringe-wash function which accounts for spatial decorrelation effects, $t = \mathbf{u}_{kl}\boldsymbol{\xi}/f_o$ is the spatial delay, and f_o is the central frequency of observation.

Remark. In the asymptotic narrow-band case, when decorrelation effects are negligible, $\widetilde{r}_{kl}(t) = 1$. Thus, if in addition all the antennae have the same radiation pattern, equation (2) reduces to the Fourier transform (1).

The modelling of the antennae and receivers used for the simulations presented in section 5 are given below. They depend on parameters whose values are given in Tables 1 and 2 and which differ from one element to another. The values of the parameters of the antennae voltage patterns are taken from measurements on the SMOS demonstrator during Avignon ground campaign [8], while those of the receivers band-pass filters are derived from Gaussian filters [9].

2.1 Antenna voltage pattern

The voltage pattern of each antenna of the interferometer is characterized by its directivity $D(\theta,\phi)$ and its phase $\Delta\varphi(\theta,\phi)$ in the viewing direction (θ,ϕ) [3]:

$$F(\theta,\phi) = D(\theta,\phi)\,\mathrm{e}^{\mathrm{j}\,\Delta\varphi(\theta,\phi)}. \tag{3}$$

In the simulations presented in section 5, the directivity obeys a power law:

$$D(\theta,\phi) = D(0)\left(\cos^{n_1}\theta\cos^2\phi + \cos^{n_2}\theta\sin^2\phi\right), \tag{4}$$

with

$$D(0) = \sqrt{\frac{2(n_1+1)(n_2+1)}{n_1+n_2+1}} \quad \text{and} \quad \begin{cases} n_1 = -0.15/\log\cos\dfrac{\theta_1}{2} \\ n_2 = -0.15/\log\cos\dfrac{\theta_2}{2} \end{cases} \tag{5}$$

where θ_1 and θ_2 are the half-power beamwidth with respect to ξ_1 and ξ_2, respectively. Likewise, the phase is varying as a function of (θ, ϕ):

$$\Delta\varphi(\theta,\phi) = \frac{2\pi}{\lambda_o}\Big(\big(D_1^{//}\sin\theta + D_1^{\perp}(1-\cos\theta)\big)\cos^2\phi + \big(D_2^{//}\sin\theta + D_2^{\perp}(1-\cos\theta)\big)\sin^2\phi\Big), \quad (6)$$

where $D_1^{//}$, $D_1^{\perp}$ and $D_2^{//}$, $D_2^{\perp}$ are the equivalent transverse and longitudinal defocussings with respect to ξ_1 and ξ_2, respectively, and λ_o is the central wavelength of observation.

Thus, each antenna voltage pattern depends on a set of six parameters which differ from one antenna to another, as illustrated in Table 1. Moreover these parameters can deviate from the calibrated or measured values, and thus contribute to errors in the modelling of the instrument [10].

Table 1: Antenna voltage pattern parameters.

	θ_1 (deg)	θ_2 (deg)	$D_1^{//}$ (mm)	$D_1^{\perp}$ (mm)	$D_2^{//}$ (mm)	$D_2^{\perp}$ (mm)
1	64.57	59.34	0.0	19.0	2.8	-30.0
2	56.00	64.00	-3.0	1.0	1.0	-25.0
3	66.47	60.77	0.0	20.0	0.0	-16.0
4	62.28	72.57	-4.0	20.0	0.5	-7.0
5	67.89	57.44	4.0	15.0	2.0	-25.0
6	62.28	67.43	0.0	22.0	1.0	-16.0
7	66.28	68.00	4.0	25.0	2.0	-9.0
8	64.57	64.57	-1.0	25.0	1.0	-12.0
9	67.43	68.57	0.0	25.0	2.0	-6.0
10	59.43	62.28	1.0	11.0	-3.0	-25.0

2.2 Receiver band-pass filter

The fringe-wash function which takes into account decorrelation effects depends on the normalized frequency responses of the receivers [3]:

$$\widetilde{r}_{kl}(t) = \frac{1}{\sqrt{B_k B_l}} \int_{-\infty}^{+\infty} H_k(f-f_o)\overline{H}_l(f-f_o)\, \mathrm{e}^{+2\mathrm{j}\pi f t}\, \mathrm{d}f, \quad (7)$$

where $H_k(f)$ and $H_l(f)$ are normalized band-pass filters so that their maximum amplitude is equal to one, B_k and B_l are their equivalent bandwidth and f_o is the central frequency of the interferometer. The band-pass filters used in the simulations presented in section 5 are ideal band-pass ones with linear phase:

$$H(f) = \mathrm{rect}(\frac{f-\bar{f}}{B})\, \mathrm{e}^{-\mathrm{j}(2\pi\tau(f-\bar{f})+\varphi)}. \quad (8)$$

Here, $\bar{f}$ and B are the central frequency and the bandwidth of the filter, τ is the group delay and φ is the phase shift. The expression of the fringe-wash function (7) for this kind of filters is established in Appendix A.

Thus, each receiver band-pass filter depends on a set of four parameters which differ from one receiver to another, as illustrated in Table 2. Here again, these parameters can deviate from the calibrated or measured values, and thus contribute to modelling errors [11].

Table 2: Receiver band-pass filter parameters.

	$\bar{f}$ (MHz)	B (MHz)	τ (nsec)	φ (deg)
1	1414.41	20.83	83	0.8
2	1414.93	19.61	79	-0.5
3	1415.54	20.25	81	-0.2
4	1414.58	19.08	80	0.3
5	1414.35	20.44	77	0.4
6	1415.29	20.62	79	-0.1
7	1415.18	19.22	82	0.2
8	1415.39	20.11	78	0.6
9	1414.27	19.84	80	-0.7
10	1415.78	19.37	77	-0.3

3 Theoretical framework

Depending on the location of the antenna elements on the array of a SAIR, the spatial frequencies $\mathbf{u}_{kl}$ for which the interferometric measurements are obtained may coincide with the nodes of a sampling grid. Moreover, since SAIR have limited physical dimensions these frequencies are always confined to a limited region H of the Fourier domain: the so-called experimental frequency coverage. As outlined in the introduction, this is the case of the SMOS instrument where the complex visibilities are obtained from raw data inside a star-shaped window over an hexagonally sampled grid [2]. Hexagonal processing is therefore here the natural way of performing synthetic aperture imaging [5]. However, another geometry may lead to another shape for H, on a Cartesian sampling grid for example.

3.1 Sampling grids

Let us consider the periodic lattice $\mathcal{H}$ extending the experimental frequency coverage H,

$$\mathcal{H} = \left\{ \mathbf{u}_{\mathbf{q}} = q_1 \mathbf{u}^{(1)} + q_2 \mathbf{u}^{(2)}, \mathbf{q} = (q_1, q_2) \in \mathbb{Z}^2 \right\} , \tag{9}$$

where the two basic translation vectors of this periodic lattice, $\mathbf{u}^{(1)}$ and $\mathbf{u}^{(2)}$, are such that $\|\mathbf{u}^{(1)}\| = \|\mathbf{u}^{(2)}\| = \delta u = d/\lambda_o$ (d is the spacing between each antenna, and λ_o is the central wavelength of observation). In the remainder of this report, n is a power of 2 such that the experimental frequency coverage H is contained in the elementary cell of

$$n\mathcal{H} = \left\{ \mathbf{U}_{\mathbf{Q}} = Q_1 \mathbf{U}^{(1)} + Q_2 \mathbf{U}^{(2)}, \mathbf{Q} = (Q_1, Q_2) \in \mathbb{Z}^2 \right\} . \tag{10}$$

Here, the two translation vectors of this periodic lattice, $\mathbf{U}^{(1)} = n\mathbf{u}^{(1)}$ and $\mathbf{U}^{(2)} = n\mathbf{u}^{(2)}$, are such that $\|\mathbf{U}^{(1)}\| = \|\mathbf{U}^{(2)}\| = \Delta u = n\,\delta u$.

To illustrate equations (9) and (10), an elementary cell of $n\mathcal{H}$ sampled at the nodes of $\mathcal{H}$ is shown in Figure 2 for the SMOS case. Here, in a Cartesian frame, $\mathbf{u}^{(1)} = (\delta u\,\sqrt{3}/2, -\delta u/2)$ and $\mathbf{u}^{(2)} = (0, \delta u)$. The areas $\sigma_{\mathbf{u}}$ and $\sigma_{\mathbf{U}}$ of the elementary cells $\mathcal{C}(\mathcal{H})$ and $\mathcal{C}(n\mathcal{H})$ of these hexagonal periodic lattices are equal to $(\delta u)^2\sqrt{3}/2$ and $(\Delta u)^2\sqrt{3}/2$, respectively.

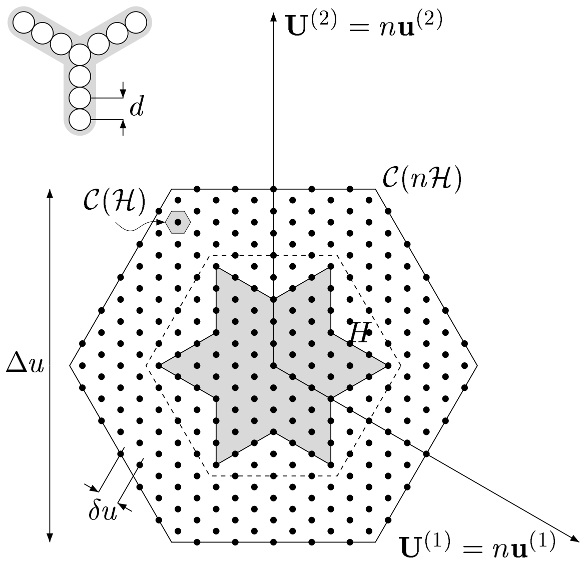

Figure 2: Elementary cell of $n\mathcal{H}$ sampled at the nodes of $\mathcal{H}$, and experimental frequency coverage H provided by a Y-shaped array with 3 equi-spaced antennae per arm in addition to the central one. Here, n has been taken equal to 16 so that the experimental frequency coverage H is contained in the elementary cell of $n\mathcal{H}$: $\delta u = d/\lambda_o$ is the Fourier sampling interval, and $\Delta u = n\,\delta u$ is the spectral bandwidth. The dashed hexagon is the smallest hexagon containing H: the smallest value for n is therefore here equal to 10.

Let now $\mathcal{H}^*$ be the reciprocal lattice of $\mathcal{H}$:

$$\mathcal{H}^* = \left\{ \Xi_{\mathbf{P}} = P_1\Xi^{(1)} + P_2\Xi^{(2)}, \mathbf{P} = (P_1, P_2) \in \mathbb{Z}^2 \right\} . \tag{11}$$

The two translation vectors $\Xi^{(1)}$ and $\Xi^{(2)}$ are such that $\|\Xi^{(1)}\| = \|\Xi^{(2)}\| = \Delta\xi$, where $\Delta\xi$ plays the dual role of δu. According to the definition of reciprocal lattices, they satisfy the following orthogonality relations: $\Xi^{(1)} \cdot \mathbf{u}^{(1)} = \Xi^{(2)} \cdot \mathbf{u}^{(2)} = 1$ and $\Xi^{(1)} \cdot \mathbf{u}^{(2)} = \Xi^{(2)} \cdot \mathbf{u}^{(1)} = 0$. In what follows, the elementary cell of $\mathcal{H}^*$ is sampled at the nodes of $\mathcal{H}^*/n$, the reciprocal lattice of $n\mathcal{H}$:

$$\mathcal{H}^*/n = \left\{ \boldsymbol{\xi}_{\mathbf{p}} = p_1\boldsymbol{\xi}^{(1)} + p_2\boldsymbol{\xi}^{(2)}, \mathbf{p} = (p_1, p_2) \in \mathbb{Z}^2 \right\} . \tag{12}$$

The vectors $\boldsymbol{\xi}^{(1)} = \Xi^{(1)}/n$ and $\boldsymbol{\xi}^{(2)} = \Xi^{(2)}/n$ are such that $\|\boldsymbol{\xi}^{(1)}\| = \|\boldsymbol{\xi}^{(2)}\| = \delta\xi = \Delta\xi/n$, where $\delta\xi$ plays the reciprocal role of Δu. They also satisfy the following orthogonality relations: $\boldsymbol{\xi}^{(1)} \cdot \mathbf{U}^{(1)} = \boldsymbol{\xi}^{(2)} \cdot \mathbf{U}^{(2)} = 1$ and $\boldsymbol{\xi}^{(1)} \cdot \mathbf{U}^{(2)} = \boldsymbol{\xi}^{(2)} \cdot \mathbf{U}^{(1)} = 0$.

To illustrate equations (11) and (12), an elementary cell of $\mathcal{H}^*$ sampled at the nodes of $\mathcal{H}^*/n$ is shown in Figure 3 for the SMOS instrument. Here, in the same Cartesian frame, $\boldsymbol{\xi}^{(1)} = (\delta\xi, 0)$ and $\boldsymbol{\xi}^{(2)} = (\delta\xi/2, \delta\xi\sqrt{3}/2)$. The areas $\sigma_{\boldsymbol{\xi}}$ and σ_{Ξ} of the elementary

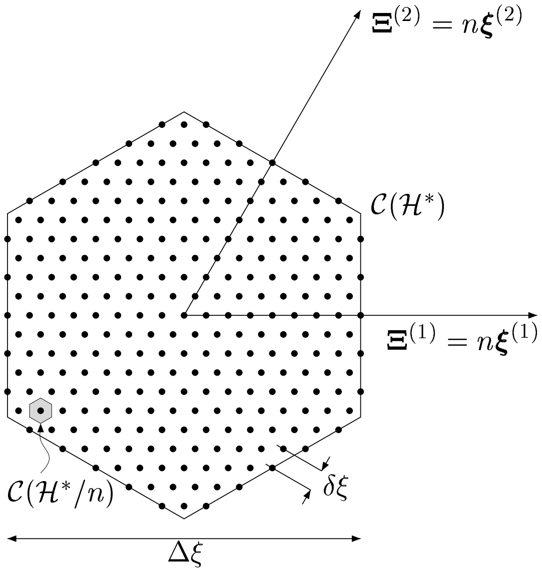

Figure 3: Elementary cell of $\mathcal{H}^*$ sampled at the nodes of $\mathcal{H}^*/n$. Here again, n has been taken equal to 16, $\delta\xi$ is the resolution scale, and $\Delta\xi = n\,\delta\xi$ is the field extension.

cells $\mathcal{C}(\mathcal{H}^*/n)$ and $\mathcal{C}(\mathcal{H}^*)$ of these hexagonal periodic lattices are equal to $(\delta\xi)^2\sqrt{3}/2$ and $(\Delta\xi)^2\sqrt{3}/2$, respectively.

According to a well-known property of reciprocal lattices, the product of the areas of the elementary cells of two reciprocal lattices is equal to unity: $\sigma_{\mathbf{u}}\,\sigma_{\mathbf{\Xi}} = \sigma_{\mathbf{U}}\,\sigma_{\boldsymbol{\xi}} = 1$. As a consequence, δu and $\Delta\xi$, and therefore Δu and $\delta\xi$, are related one to another. Substituting for the expressions of these areas, we therefore have in the special case of hexagonal periodic lattices,

$$\Delta\xi\,\delta u = \Delta u\,\delta\xi = \frac{2}{\sqrt{3}} \quad \text{with} \quad \begin{cases} \Delta\xi = n\,\delta\xi, \\ \Delta u = n\,\delta u. \end{cases} \tag{13}$$

In the context of synthetic aperture imaging, these relations show that both the Fourier sampling interval δu and the spectral bandwidth Δu, are related to the resolution scale $\delta\xi$ and to the field extension $\Delta\xi$. This remark also holds for Cartesian periodic lattices. In such a case, these relations will reduce to $\Delta\xi\,\delta u = \Delta u\,\delta\xi = 1$.

Let us finally introduce the two sets of n^2 integers,

$$\mathbb{G}(n\mathcal{H}) = \left\{\mathbf{q} \in \mathbb{Z}^2 : \mathbf{u}_{\mathbf{q}} \in \mathcal{C}(n\mathcal{H})\right\}. \tag{14}$$

$$\mathbb{G}(\mathcal{H}^*) = \left\{\mathbf{p} \in \mathbb{Z}^2 : \boldsymbol{\xi}_{\mathbf{p}} \in \mathcal{C}(\mathcal{H}^*)\right\}, \tag{15}$$

As $\mathcal{C}(\mathcal{H}^*)$ is sampled at the nodes of $\mathcal{C}(\mathcal{H}^*/n)$, $\mathbb{G}(\mathcal{H}^*)\,\delta\xi$ is none other than the finite spatial grid represented in Figure 3. The area of the pixels of this grid is of course equal to $\sigma_{\boldsymbol{\xi}}$. Likewise, $\mathbb{G}(n\mathcal{H})\,\delta u$ is the finite Fourier grid represented in Figure 2, here the area of the elementary cell $\mathcal{C}(\mathcal{H})$ is of course equal to $\sigma_{\mathbf{u}}$.

Remark. Here the integer n has been chosen to be a power of 2 for forthcoming computational reasons. However, provided that the Shannon sampling criterion is satisfied, this condition can be of course relaxed and the size of the hexagonal dual grids $\mathbb{G}(\mathcal{H}^*)\,\delta\xi$ and $\mathbb{G}(n\mathcal{H})\,\delta u$ modified accordingly.

3.2 Working spaces

The object workspace E is the finite-dimensional space in which the Fourier synthesis operation is performed with the aid of the computer [12][13]. Here it is the space of the functions T that take their values $T_{\mathbf{p}} \equiv T(\boldsymbol{\xi}_{\mathbf{p}})$ on the nodes $\boldsymbol{\xi}_{\mathbf{p}}$ of the spatial grid $\mathbb{G}(\mathcal{H}^*)\,\delta\xi$. The dual workspace $\widehat{E}$ is the image of E by the Fourier transform operator. Clearly, it is the space of the Fourier transforms $\widehat{T}$ that take their values $\widehat{T}_{\mathbf{q}} \equiv \widehat{T}(\mathbf{u}_{\mathbf{q}})$ on the nodes $\mathbf{u}_{\mathbf{q}}$ of the Fourier grid $\mathbb{G}(n\mathcal{H})\,\delta u$.

The H-band limited functions $\mathcal{T}$, defined as those having their Fourier transform $\widehat{\mathcal{T}}$ confined to the experimental frequency coverage H, play an important role in Fourier synthesis [13]. They belong to a subspace $\mathcal{E}$ of E, the image of which by the Fourier transform operator is a subspace $\widehat{\mathcal{E}}$ of $\widehat{E}$. The functions $\widehat{\mathcal{T}}$ take their values $\widehat{\mathcal{T}}_{\mathbf{q}} \equiv \widehat{\mathcal{T}}(\mathbf{u}_{\mathbf{q}})$ on the nodes $\mathbf{u}_{\mathbf{q}}$ of the Fourier grid which only belong to H.

The spatial frequencies $\mathbf{u}_{kl}$ associated to antennae A_k and A_l in (1) and (2) belong to a finite list $\mathcal{L}$ in the Fourier domain: $\mathcal{L} = \{\mathbf{u}_{kl} : 1 \leq k, l \leq \ell\}$, where ℓ is the number of antennae of the interferometer. This list may be redundant: two different pairs of antennae may lead to the same spatial frequency. According to (1) and (2), the data space F is the space of the hermetian complex-valued functions V that take their values $V_{kl} \equiv V(\mathbf{u}_{kl})$ on $\mathcal{L}$.

Remark. According to the hermitian property of the Fourier transform of real-valued functions, and to the one of the complex visibilities, whether they are related to the brightness temperature by (1) or (2), the dual spaces $\widehat{E}$ and $\widehat{\mathcal{E}}$ might have been defined on only half of the nodes of the grids used. The same remark holds for the data space F and the experimental frequency list $\mathcal{L}$. However, to introduce these spaces and their inner products comfortably, it was preferable to make this remark at the end rather than to introduce an additionnal difficulty, and therefore some confusion, in their definition.

3.3 Key operators

Let us first introduce the discrete Fourier transform operator $\mathbf{U}$:

$$\begin{array}{rcl} \mathbf{U} : E & \longrightarrow & \widehat{E} \\ T & \longmapsto & \mathbf{U}T = \widehat{T} \end{array}$$

with, for any $\mathbf{q}$ in $\mathbb{G}(n\mathcal{H})$:

$$\widehat{T}_{\mathbf{q}} = \sigma_{\boldsymbol{\xi}} \sum_{\mathbf{p} \in \mathbb{G}(\mathcal{H}^*)} T_{\mathbf{p}}\, \mathrm{e}^{-2\mathrm{j}\pi \dfrac{\mathbf{p} \cdot \mathbf{q}}{n}} \,. \tag{16}$$

In the case of hexagonal grids, it has been shown [14] that these computations can be performed with the aid of a standard FFT algorithm, thus making unnecessary the development of an algorithm tailored to hexagonal grids [15].

Remark. Following the remark made in section 3.1, another solution [5] has been proposed for using rectangular FFT routines (eq. (23) in [5]), however standard radix-2 FFT algorithm cannot be used since the number of pixels in the hexagonal grids is taken equal to ℓ^2, the square of the total number of antennae which is generally not a power of 2.

Let now $\mathbf{Z}$ be the zero-padding operator beyond the experimental frequency coverage H:

$$\begin{array}{rcl} \mathbf{Z} : \widehat{\mathcal{E}} & \longrightarrow & \widehat{E} \\ \widehat{\mathcal{T}} & \longmapsto & \mathbf{Z}\widehat{\mathcal{T}} = \widehat{T} \end{array}$$

with, for any $\mathbf{q}$ in $\mathbb{G}(n\mathcal{H})$:

$$\widehat{T}_{\mathbf{q}} = \begin{cases} \widehat{\mathcal{T}}_{\mathbf{q}} & \text{if } \mathbf{u}_{\mathbf{q}} \in H, \\ 0 & \text{otherwise.} \end{cases} \tag{17}$$

The action of its adjoint, $\mathbf{Z}^*$, which consists in keeping only the components $\widehat{T}_{\mathbf{q}}$ of $\widehat{T}$ inside H, is therefore such that $\mathbf{Z}^*\mathbf{Z} = \mathbf{I}$. Consequently, the action of the operator

$$\mathbf{P}_H = \mathbf{U}^*\mathbf{Z}\mathbf{Z}^*\mathbf{U} \tag{18}$$

is that of a projector onto the space $\mathcal{E}$ of the H-band limited functions since it is straightforward to prove that $\mathbf{P}_H^* = \mathbf{P}_H$ and $\mathbf{P}_H^2 = \mathbf{P}_H$.

Finally, the modelling operator is the operator $\mathbf{G}$ from the object workspace E into the data space F describing the basic relationship (2) between the complex visibility samples and the brightness temperature distribution of the scene under observation:

$$\begin{array}{rcl} \mathbf{G} : E & \longrightarrow & F \\ T & \longmapsto & \mathbf{G}T = V \end{array}$$

with, for any antennae pair A_k and A_l:

$$V_{kl} = \sigma_{\boldsymbol{\xi}} \sum_{\mathbf{p} \in \mathbb{G}(\mathcal{H}^*)} \frac{F_{k,\mathbf{p}}\, \overline{F}_{l,\mathbf{p}}}{\sqrt{1 - ||\boldsymbol{\xi}_{\mathbf{p}}||^2}}\, T_{\mathbf{p}}\, \widetilde{r}_{kl}\left(\frac{-\mathbf{u}_{kl}\boldsymbol{\xi}_{\mathbf{p}}}{f_o}\right) \mathrm{e}^{-2\mathrm{j}\pi \mathbf{u}_{kl}\boldsymbol{\xi}_{\mathbf{p}}}. \tag{19}$$

The action of the adjoint of $\mathbf{G}$ is established in Appendix B.

For computation purposes, numerical quadrature has been used to represent (2) as a summation over n^2 integrand samples, the n^2 elementary cells $\mathcal{C}(\mathcal{H}^*/n)$ of the spatial grid $\mathbb{G}(\mathcal{H}^*)\,\delta\xi$. Here again, n is chosen in such a way that the Shannon sampling criterion is satisfied and the numerical quadrature is sufficiently accurate. Shown in Figure 4 are the variations of the relative error on the numerical computation of $V(\mathbf{0})$ with n. Since the temperature of the test scene is here constant and equal to $T_o/4\pi$ all over the space, the theoretical visibility for the zero spacing is equal to T_o [7]. With the smallest number of integrand samples the corresponding modelling error is approximately equal to 0.25%, that is to say 0.75 K for $T_o = 300$ K, but it can be significantly reduced by simply working at a higher level of discretization. Since the numerical quadrature is performed with the aid of a trapezoidal rule, the behavior of these variations is not surprising and must be kept in mind since (19) is the relation to be inverted to retrieve the radiometric brightness temperature of the scene under observation from experimental complex visibilities.

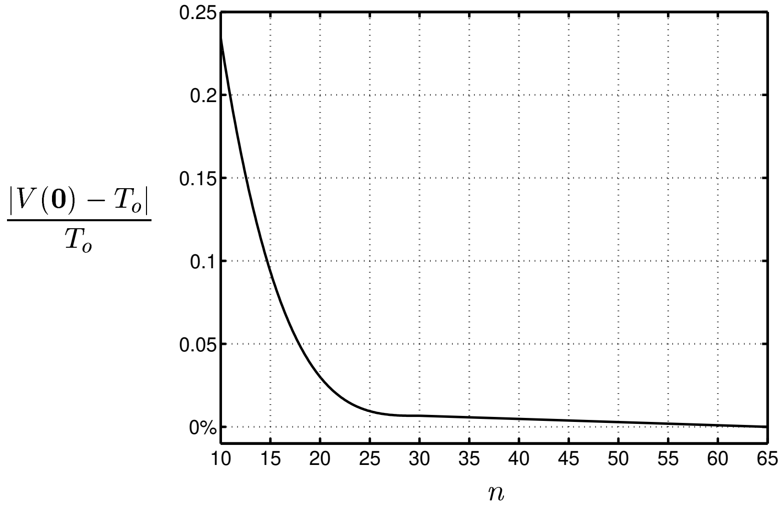

Figure 4: Variations of the relative error on the computation of $V(\mathbf{0})$ with the level of discretization of the numerical quadrature used to represent the integral modelling the instrument with a trapezoidal rule. Since the Y-shaped array used for these numerical integrations is equipped with 10 antennae (the parameters of which are listed in Table 1), the relative error ploted here as a function of n (n^2 is the number of integrand samples), is the average of the values computed for the 10 antennae. The theoretical visibility for the zero spacing is equal to T_o. At the smallest level of discretization, $n = 10$ (see Figure 2), the modelling error is approximately equal to 0.25%, that is to say 0.75 K for $T_o = 300$ K.

4 Inverse problem

The problem addressed in this working note is to retrieve an estimate of the radiometric brightness temperature distribution from a set of measured complex visibilities. Clearly, since the *direct problem* is stated via an integral equation, namely (2), the *inverse problem* does not usually have a straightforward solution. This kind of problem, which is certainly not unique to microwave remote sensing [16], may be solved through the application of inversion techniques [17], and as far as possible with the aid of the most up-to-date algorithms in numerical analysis [18].

4.1 Band limited imaging device

Referring back to Figure 1, the only spatial frequencies $\mathbf{u}_{kl}$ for which interferometric measurements are made are those corresponding to antennae pairs A_k and A_l. Since SAIR have limited physical dimensions, the discrete version of (1) is not a Fourier transform between the visibility samples $V(\mathbf{u}_{kl})$ and the so-called "modified brightness temperature" $\widetilde{T}(\boldsymbol{\xi}) = |F(\boldsymbol{\xi})|^2 T(\boldsymbol{\xi})/\sqrt{1 - \|\boldsymbol{\xi}\|^2}$ [5]. Indeed, in such a case the action of $\mathbf{G}$ on T is that of $\mathbf{Z}^*\mathbf{U}$ on $\widetilde{T}$, not that of $\mathbf{U}$, because the spatial frequencies $\mathbf{u}_{kl}$ in $\mathcal{L}$ belong to H. It is therefore illusive to expect retrieving with the aid of a simple inverse Fourier transform the original distribution of $\widetilde{T}$ at its highest level of resolution because its Fourier components beyond H are lost. As a consequence, only a smoothed version of $\widetilde{T}$, and therefore of T, can be retrieved through the reconstruction operator $\mathbf{U}^*\mathbf{Z}$ which is not the inverse of $\mathbf{Z}^*\mathbf{U}$. Indeed, $\mathbf{U}^*\mathbf{Z}\mathbf{Z}^*\mathbf{U}$ is not the identity operator: it is the projector $\mathbf{P}_H$ onto the space $\mathcal{E}$ of the H-band limited functions (18). This is why SAIR are band-limited imaging devices [17].

When the instrument modelling is given by (2), $\widetilde{T}$ is not defined when the antennae have different voltage patterns, unless an average one has a physical meaning. Moreover, the $\mathbf{U}^*\mathbf{Z}$ reconstruction requires to average the redundant visibilities, or to select one out of them (the former being better since it increases the signal to noise ratio in presence of random errors). Consequently, it could not account for either imperfections of the subsystems of the interferometer or for decorrelation effects. We aim in here at retrieving the brightness temperature distribution that would have been reconstructed from visibility samples provided by an ideal SAIR at the same level of resolution. Of course, this has to be done by taking into account all the information available, without averaging the redundant one.

4.2 Ill-posedness of the inverse problem

Since the dimension of the object workspace E is larger than the dimension of the data space F, because the number of pixels in the spatial grid $\mathbb{G}(\mathcal{H}^*)\,\delta\xi$ is much larger than the number of spatial frequencies in $\mathcal{L}$, the linear system $\mathbf{G}T = V$ is an underconstrained problem. As a consequence, there are multiple solutions for T. According to the definition given by Hadamard (chap. 1 in [17]), this inverse problem is therefore ill-posed.

Remark. Working at a level of discretization such that the matrix $\mathbf{G}$ becomes a square one cannot eliminate the problem. Following the remark made in section 3.3, this requires to set the number of pixels n^2 in the hexagonal grids to the square of the total number of antennae ℓ^2. Since the number of visibilities is equal to $\ell(\ell-1)$, the total power measurements provided by the ℓ antennae have to be included in the modelling operator. However, not all SAIR are functionning this way. Indeed, some may provide only one antenna dedicated to the measurement of $V(\mathbf{0})$, and considering this measurement ℓ times leads to a singular square matrix.

One approach [19] is to ignore the ill-posedness of the problem and to use an iterative method to select one solution out of the potential many ones. The solution thus obtained depends on the starting point of the iterative method and also on the number of iterations performed. However, in such a case, it is important to keep in mind the behavior of the successive-approximations method: when the number of iterations increases, the iterates first approach one solution and then may drift to a neighbouring one as the result of a numerical instability (chap. 6 in [17]). It is therefore necessary to perform only a few number of iterations. This is exactly what is reported in the illustration of the modified Clean algorithm in [19]: the iterative process is initialized with a brightness temperature obtained from the zero-padded inverse Fourier transform of the averaged visibilities divided by an average antenna power pattern, and only 2 to 7 iterations are performed. Since the linear system to be solved has 16900 unknowns, this very small number of iterations can only provide a solution close to the initial guess. This method is very efficient for an instrument with small discrepancies between antennae patterns and with small decorrelation effects, otherwise averaging may not be the best way to take into account all the available information.

Remark. As argued in [19], working with differential visibilities for which known contributions from the cold sky and the Earth are removed from the experimental measurements expands the alias-free field of view and reduces the Gibbs phenomenon introduced by the Earth aliases. However, this approach does not regularize the problem at all, since it modifies only the right-hand side of the linear system $\mathbf{G}T = V$ while the ill-posedness of the problem is inherent in the modelling operator $\mathbf{G}$ and in the objective to solve for T, not in the data V (chap. 5 in [17]).

Another approach [20] is to find the minimum norm solution $T_r = \mathbf{G}^+ V$ by means of computing the Moore-Penrose pseudo-inverse $\mathbf{G}^+$ of the rectangular matrix $\mathbf{G}$ with an appropriate method [21]. According to Parseval's theorem, the norm of T_r is equal to the norm of $\widehat{T}_r$. The minimum norm solution will therefore have a large fraction of its energy in the Fourier domain concentrated in the experimental frequency coverage H. As a consequence, it will not differ much from an H-band limited solution (this remark will be illustrated in section 5). However, from the numerical analysis point of view, this solution cannot be computed without any difficulty when the matrix $\mathbf{G}$ is badly conditioned, or when it is rank deficient. Indeed, in such a case $\mathbf{G}^+$ cannot be calculated with the well-known expression $\mathbf{G}^*(\mathbf{G}\mathbf{G}^*)^{-1}$ since the inverse of $\mathbf{G}\mathbf{G}^*$ is not defined. This situation is encountered as soon as two redundant baselines are associated to identical subsystems. In such a case the matrix $\mathbf{G}$ exhibits linearly dependant rows and is of course rank deficient. Then, only one of these rows should be kept in the inversion and the visibilities corresponding to the discarded rows have to be ignored or averaged. Averaging is of course better, but one consequence of this situation is to decrease the ratio between the amount of information and the number of unknowns of a linear system which is already underconstrained. The best approach is to compute $\mathbf{G}^+$ with the aid of a truncated singular value decomposition (TSVD), so that the smallest singular values of $\mathbf{G}$ are properly treated prior to inversion (chap. 3 and 5 in [21]). The impact of these singular values on the stability of T_r will be illustrated in section 5.

The approach presented in the next section consists in curing the ill-posedness of the problem. Indeed, the situation can be summarized by the words of Twomey in the preface of his book [16], "The crux of the difficulty was that numerical inversions were producing results which were physically unacceptable but were mathematically acceptable." Therefore, the inverse problem $\mathbf{G}T = V$ has to be regularized in order to reduce the set of the solutions compatible both with the experimental visibilities and with the instrument modelling, and also to discriminate between solutions generated by uncontrolled propagation of various errors. When investigating the propagation of errors ΔV from the data V to a solution T_r, the standard analysis (chap. 1 in [22]) provides the following estimation:

$$\frac{\|\Delta T_r\|_E}{\|T_r\|_E} \leq \mathcal{C}(\mathbf{G}) \frac{\|\Delta V\|_F}{\|V\|_F}. \tag{20}$$

Here, $\mathcal{C}(\mathbf{G})$, which is the condition number of the inverse problem $\mathbf{G}T = V$ with respect to perturbations on the right-hand side V, is an upper bound for the amplification factor of errors. As illustrated in section 5, this factor may be larger than the effective amplification factor.

4.3 Regularization of the inverse problem

As outlined in section 4.1, SAIR instruments are band-limited imaging devices. It results that the inverse problem $\mathbf{G}T = V$ is ill-posed as a consequence of the loss of information beyond the experimental frequency coverage H. Additional information is therefore necessary in order to compensate this irreversible loss. Such information, which is also termed *a priori* or *prior information*, is additional in the sense that it cannot be derived from the visibilities themselves, but should express some expected physical properties of the brightness temperature and/or of the imaging radiometer.
Since SAIR do not transmit any information outside H, it is physically legitimate to search for the reconstructed brightness temperature in the space of the H-band limited functions [12]. In other words, the limited angular resolution of the SAIR is here taken into account, and the appropriate solution to the inverse problem is a temperature field constrained in such a way that it does not exhibit features at a resolution finer than this physical limit. The regularized solution is thus defined as the function minimizing the discrepancy functional:

$$\min_{T \in E} \|V - \mathbf{G}T\|_F^2, \tag{21}$$

subject to the constraint:

$$(\mathbf{I} - \mathbf{P}_H)T = 0\,, \tag{22}$$

where $\mathbf{P}_H$ is the projection operator onto the space $\mathcal{E}$ of the H-band limited functions (18). Denoting now by $\widehat{\mathcal{T}}$ the Fourier components of T inside the experimental frequency coverage H, the constraint (22) can be expressed by the relation $\mathbf{U}T = \mathbf{Z}\widehat{\mathcal{T}}$. Substituting for $T = \mathbf{U}^*\mathbf{Z}\widehat{\mathcal{T}}$ into (21) leads to the overconstrained least squares criterion:

$$\min_{\widehat{\mathcal{T}} \in \widehat{\mathcal{E}}} \|V - \mathbf{A}\widehat{\mathcal{T}}\|_F^2, \tag{23}$$

where $\mathbf{A} = \mathbf{G}\mathbf{U}^*\mathbf{Z}$. The function that realizes the minimum of (23) is also the unique solution of the normal equation:

$$\mathbf{A}^*\mathbf{A}\widehat{\mathcal{T}} = \mathbf{A}^*V. \tag{24}$$

This problem can be solved either with the aid of an iterative method (chap. 7 in [22]), or with a direct one (chap. 3 and 5 in [18]). Since the square matrix $\mathbf{A}^*\mathbf{A}$ is not singular (because the inverse problem has been regularized), we obtain therefrom the H-band limited solution $T_r = \mathbf{U}^*\,\mathbf{Z}\,\widehat{\mathcal{T}}_r$ with $\widehat{\mathcal{T}}_r = (\mathbf{A}^*\mathbf{A})^{-1}\mathbf{A}^*\,V$. The rectangular matrix $\mathbf{A}^+ = (\mathbf{A}^*\mathbf{A})^{-1}\mathbf{A}^*$, which is the More-Penrose pseudo-inverse of $\mathbf{A}$, is also called the resolving matrix of the instrument. It makes the connection between the complex visibilities and the unknowns of the regularized problem, namely the Fourier transform coefficients of the reconstructed brightness temperature inside the experimental frequency coverage H.

Coming back to the propagation of errors, and therefore to the stability of the reconstruction process, here again the standard analysis provides the following estimation, similar to (20):

$$\frac{\|\Delta\widehat{\mathcal{T}}_r\|_{\widehat{\mathcal{E}}}}{\|\widehat{\mathcal{T}}_r\|_{\widehat{\mathcal{E}}}} \leq \mathcal{C}(\mathbf{A})\frac{\|\Delta V\|_F}{\|V\|_F} \tag{25}$$

where $\mathcal{C}(\mathbf{A})$, the condition number of $\mathbf{A}$ with respect to perturbations ΔV on V, has to be compared to $\mathcal{C}(\mathbf{G})$. As illustrated in the next section, the latter may be larger than the former.

Let finally note that here, the reconstructed brightness temperature has a clear physical meaning: it is the distribution that would have been reconstructed from complex visibilities provided by an ideal instrument at the resolution associated with the extension of the experimental aperture H. In a real processing case, its Fourier components in H will be damped by an appropriate real-valued centrosymetric apodization (or windowing) function W in order to filter-out the Gibbs effects due to the sharp frequency cut-off [14][23]. In the numerical simulations presented in the next section, the Hanning window shown in Figure 5 has been used. Of course, another one with different properties might have been chosen, but the aim of this note is not to discuss on the trade-off to be made between spatial resolution [23] and radiometric sensitivity [24]. Since this window is the same for all the simulations, the comparison between the different methods is significant from the point of view of their relative performances.

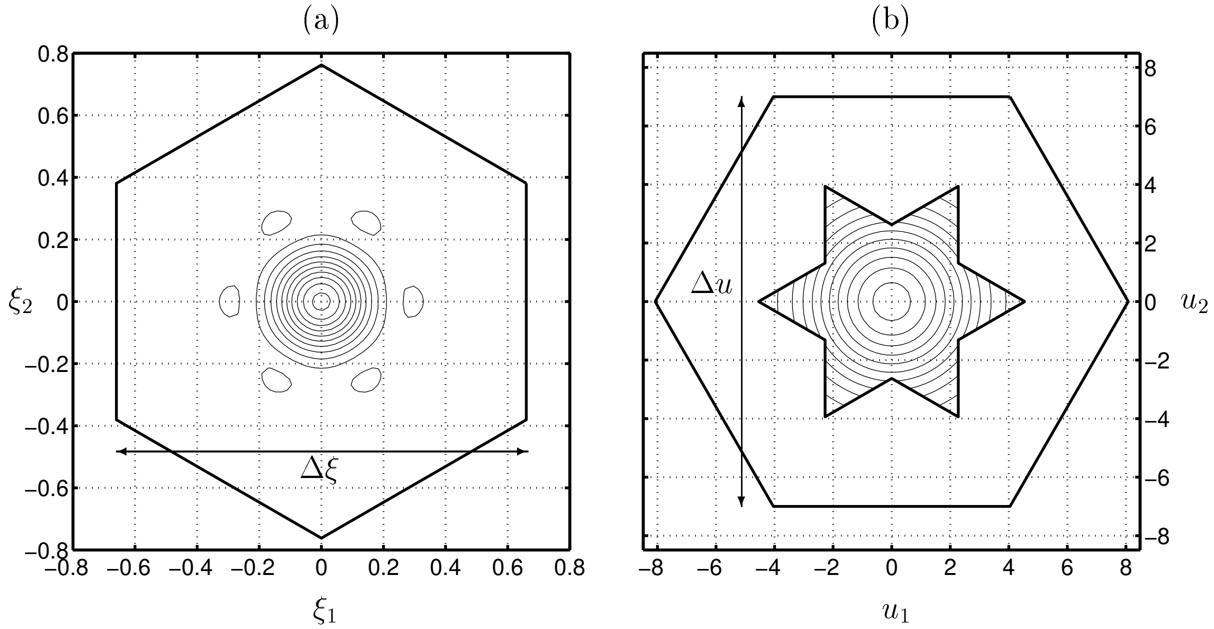

Figure 5: Hanning window $\widehat{W}(\mathbf{u})$ in the Fourier domain (b) with $\Delta u = 16\,\delta u = 14$, and the corresponding apodized point normalized spread function $W(\boldsymbol{\xi})/W(\mathbf{0})$ of the instrument in the spatial domain (a), with $\Delta\xi = 16\,\delta\xi \simeq 1.32$. Here, the full width at half maximum value, which is related to the angular resolution, is here close to $3\,\delta\xi$ (contour levels range from 0 to 1 with increments of 0.1).

5 Numerical simulations and results

Numerical simulations have been performed for a Y-shaped array equipped with 3 antennae per arm in addition to the central one, leading to a total number of antennae and receivers $\ell = 10$, and the antenna spacing d has been set to $0.875\,\lambda_o$. The number of simultaneous complex visibilities provided by this instrument is therefore equal to $\ell(\ell-1) = 90$ (45 when taking into account the hermitian property), while there are only 72 spatial frequencies in the star-shaped frequency coverage H (36 when taking into account the hermitian property). The dimension of the hexagonally sampled grids $\mathbb{G}(\mathcal{H}^*)\,\delta\xi$ and $\mathbb{G}(n\mathcal{H})\,\delta u$ has been fixed to $n = 16$. The object workspace E is thus isomorphic to $\mathbb{R}^{256}$.

Only one measurement of the visibility function for the zero spacing $V(\mathbf{0})$ has been included in the modelling operator $\mathbf{G}$. The dual space $\widehat{\mathcal{E}}$ and the data space F are therefore isomorphic to $\mathbb{C}^{36+1}$ and to $\mathbb{C}^{45+1}$, respectively. For computational reasons it is preferable to work in the underlying real spaces $\mathbb{R}^{73}$ and $\mathbb{R}^{91}$, respectively. The size of the real-valued matrix $\mathbf{G}$ is therefore 91×256 (the linear system $\mathbf{G}T = V$ is underdetermined since there are 256 unknowns for only 91 equations), while that of the real-valued matrix $\mathbf{A}$ is only 91×73 (the least square criterion (23) is overconstrained since there are only 73 unknowns for 91 equations).

The brightness temperature distribution T of the test scene chosen for the simulations is shown in Figure 6a at its highest level of resolution, and in Figure 6b at the resolution level of the Hanning window W shown in Figure 5. The latter, which is defined by the convolution relation $T_w = W \star T$, is the brightness temperature map to be reconstructed.

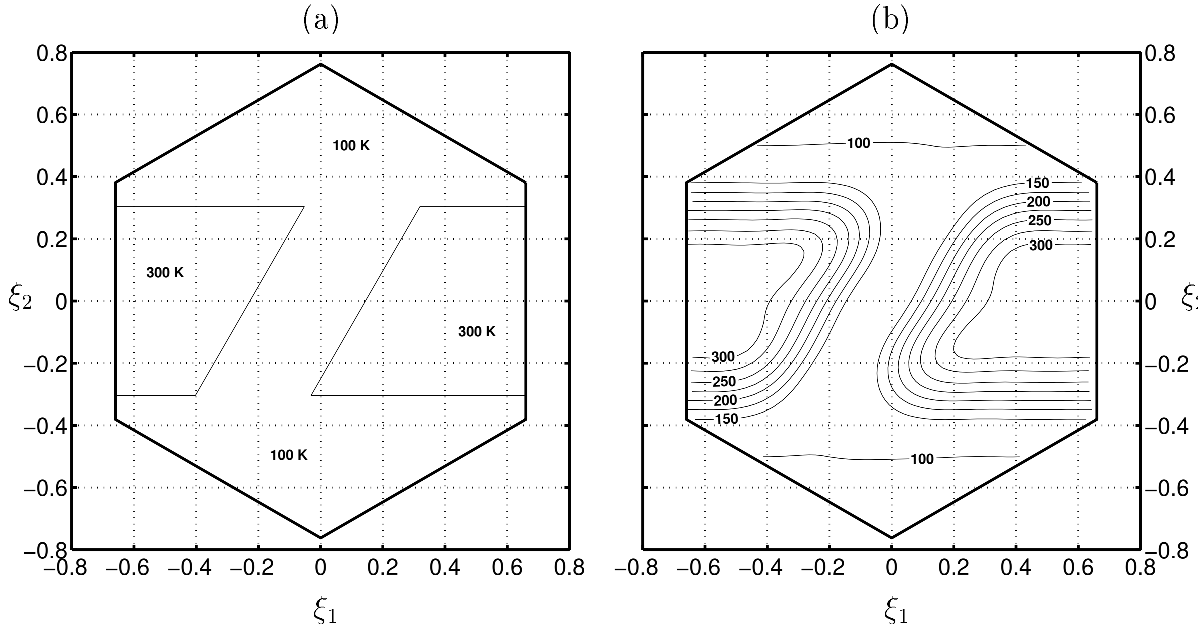

Figure 6: Brightness temperature map T of the test scene at its highest level of resolution (a) and at the level of resolution of the instrument and damped with a Hanning window $T_w = W \star T$ (b).

Indeed, as demonstrated in section 4.1, SAIR instruments are band-limited imaging devices. This statement is illustrated in Figure 7 where reconstructions are performed with the aid of the simple reconstruction operator $\mathbf{U}^*\mathbf{Z}$ for an ideal instrument equipped with identical antennae (the parameters of this antenna are those of the central one numbered 1 in Table 1) and no fringe wash effects, as well as for a real one with non identical subsystems.

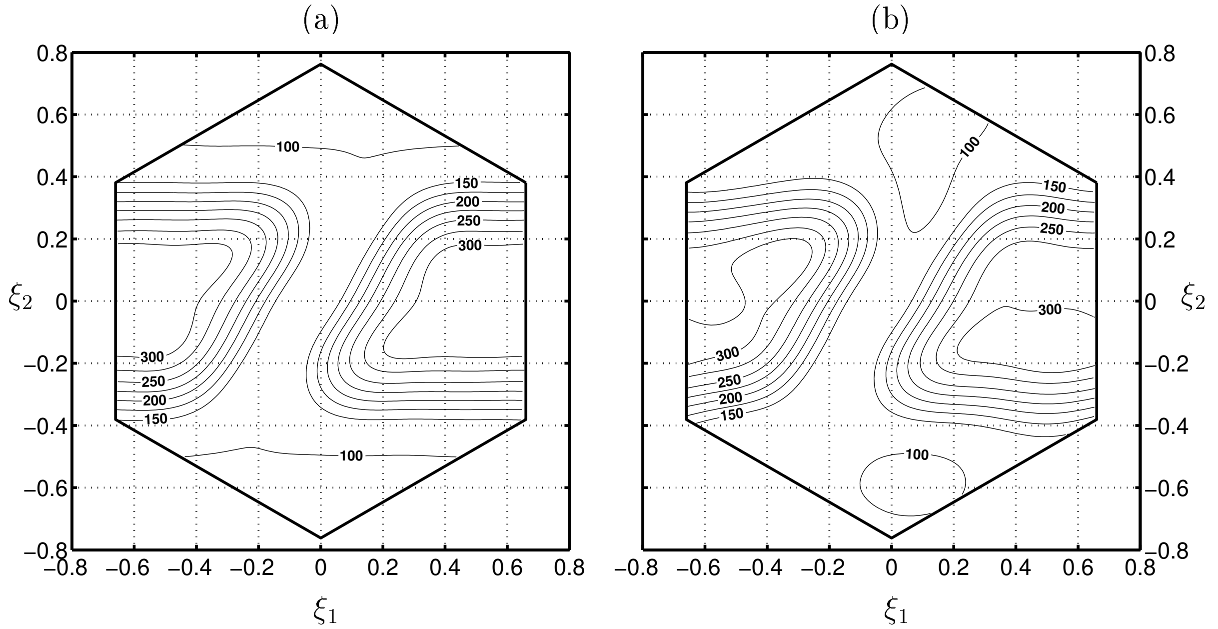

Figure 7: Brightness temperature maps T_r reconstructed with a simple inverse Fourier transform of complex visibilities computed from T at its highest level of resolution (see Figure 6a) for an ideal instrument equipped with identical antennae and no fringe wash effects (a), as well as for a real one with non identical subsystems (b). As expected, even in the case of an ideal instrument only a smoothed version of the original brightness temperature map can be retrieved. These maps have to be compared to the brightness temperature map T_w shown in Figure 6b. When the instrument is not an ideal one, in particular when fringe wash effects occur, the reconstruction, which requires to average the redundant visibilities, is not satisfactory (the rms error $\sigma^0_{\Delta T}$ between T_w and T_r is about 10 K).

As expected, even in the case of an ideal instrument, only a smoothed version of the original brightness temperature map can be retrieved: the reconstructed map thus obtained T_r has clearly to be compared to T_w, rather than to T. In agreement with predictions of section 4.1, when the instrument is not an ideal one, the effects that have not been taken into account in the reconstruction clearly appear: the reconstructed map T_r is not satisfactory.

Remark. In the real situation of an instrument viewing the Earth from an elevation h above the sea surface (see Figure 1), aliases of the Earth should appear in the reconstructed maps [5]. This is not the case here since T is limited to the instantaneous field of view of the instrument, the hexagonal cell $\mathcal{C}(\mathcal{H}^*)$, and therefore does not spread over the entire space in front of each antenna. The motivation of this choice is to concentrate on the reconstruction methods without adding an additional geometrical problem, which is independant on the reconstruction method chosen.

Complex visibilities have been simulated from the brightness temperature distribution of the test scene at its highest level of resolution for a real instrument with non identical subsystems (the parameters of which are listed in Tables 1 and 2). Reconstructions have been performed in order to compare the minimum norm solution $T_r = \mathbf{G}^+V$ of the linear system $\mathbf{G}T = V$ and the band-limited solution $T_r = \mathbf{U}^*\mathbf{Z}\mathbf{A}^+V$ of the normal equation (24).

In a first step, reconstructions have been performed from complex visibilities free from radiometric errors. As expected, there is no significant difference between the two reconstructed brightness temperature maps T_r shown in Figure 8 and the map to be reconstructed T_w shown in Figure 6b: the rms error $\sigma^{\,0}_{\Delta T}$ between T_w and T_r is here about 1.010 K for $T_r = \mathbf{G}^+V$ and 0.937 K for $T_r = \mathbf{U}^*\mathbf{Z}\mathbf{A}^+V$. This error is attributable to the high frequency components of T which have contributed to the complex visibilities V, while both reconstructions are performed at the resolution level of the instrument and apodized with the Hanning window. This error is therefore a systematic error which depends on the scene under observation T, as well as on the apodization function W and of course on the resolution level of the instrument.

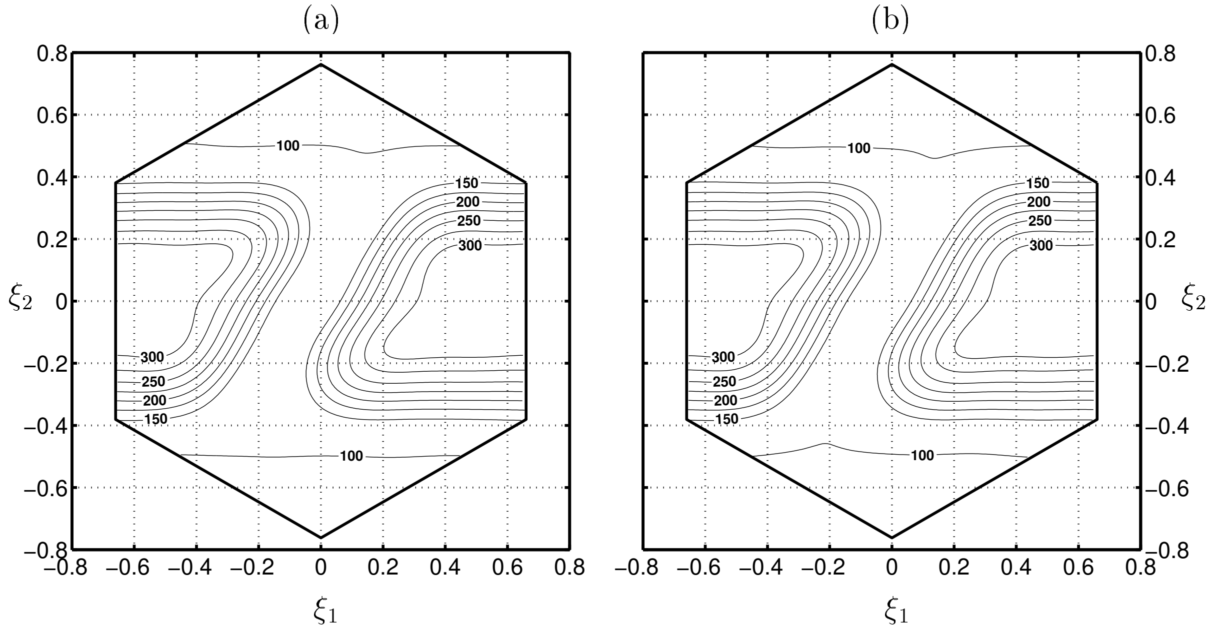

Figure 8: Brightness temperature maps T_r reconstructed with the ill-posed approach (a) and with the regularized one (b). Both maps are at the level of resolution of the apodized point spread function W shown in Figure 5, so that they can be compared to the brightness temperature map T_w shown in Figure 6b. The minumum norm solution $T_r = \mathbf{G}^+V$ (a) is obtained through the computation of the More-Penrose pseudo-inverse $\mathbf{G}^+ = \mathbf{G}^*(\mathbf{G}\mathbf{G}^*)^{-1}$, while the band-limited solution $T_r = \mathbf{U}^*\mathbf{Z}\mathbf{A}^+V$ (b) is here obtained through the computation of the resolving matrix $\mathbf{A}^+ = (\mathbf{A}^*\mathbf{A})^{-1}\mathbf{A}^*$. There is no significant differences between the two reconstructions: the rms error $\sigma^{\,0}_{\Delta T}$ between T_w and $T_r = \mathbf{G}^+V$ is here about 1.010 K, and of the order of 0.937 K between T_w andr $T_r = \mathbf{U}^*\mathbf{Z}\mathbf{A}^+V$.

In a second step, the complex visibilities were blurred by adding a complex Gaussian noise. More precisely, for all the baselines $\mathbf{u}_{kl}$ of $\mathcal{L}$, a radiometric noise ΔV with standard deviation $\sigma_{\Delta V} = (T_A + T_R)/\sqrt{B\tau_i}$ [24] on both the real and imaginary parts of V_{kl} is added, with $T_A = 250$ K, $T_R = 100$ K, $B = 20$ MHz and $\tau_i = 1$ second. These values lead to a standard deviation $\sigma_{\Delta V}$ of the order of 0.08 K. Both reconstructed maps are shown in Figure 9. In agreement with predictions, the minimum norm solution is more sensitive to input errors than the regularized one: the rms error $\sigma_{\Delta T}$ between T_w and $T_r = \mathbf{G}^+V$ is here about 2.118 K, while it is of the order of 0.938 K between T_w and $T_r = \mathbf{U}^*\mathbf{Z}\mathbf{A}^+V$. Keeping in mind that an amount $\sigma^{\,0}_{\Delta T}$ of these errors is systematic, the remaining amount $\sqrt{(\sigma_{\Delta T})^2 - (\sigma^{\,0}_{\Delta T})^2}$ which is attributable to the propagation of ΔV is therefore of the order of 1.862 K for $T_r = \mathbf{G}^+V$ and about 0.043 K for $T_r = \mathbf{U}^*\mathbf{Z}\mathbf{A}^+V$. Consequently, the amplification of the input errors is approximately 45 times larger for $\mathbf{G}^+$, 23.3 K/K, as compared to $\mathbf{U}^*\mathbf{Z}\mathbf{A}^+$, only 0.54 K/K.

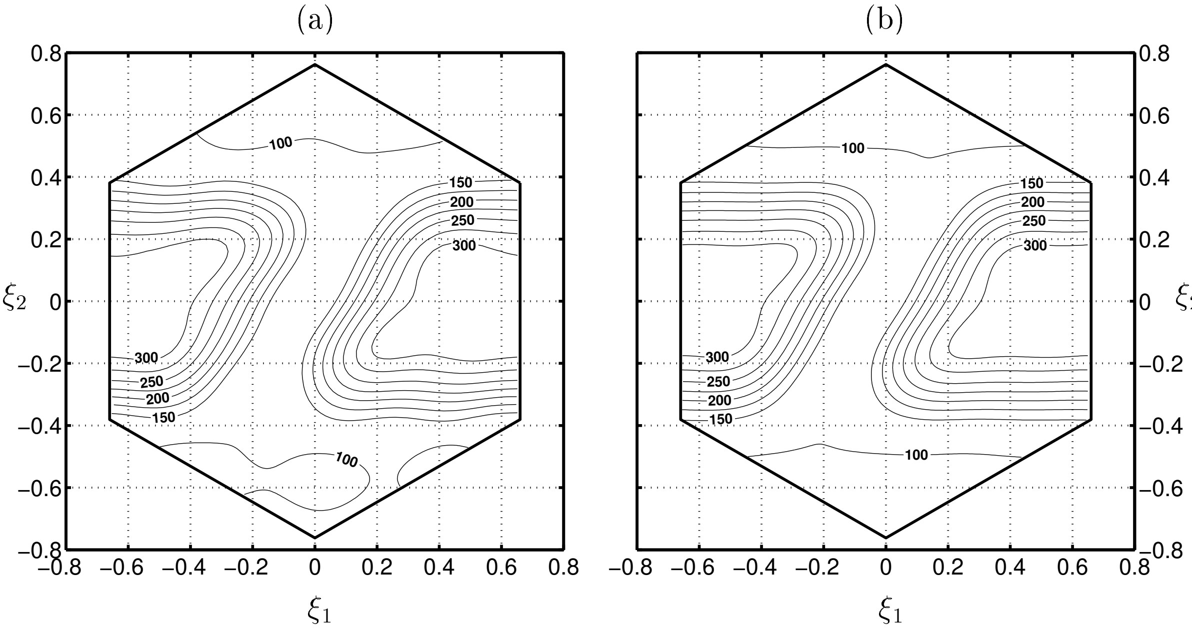

Figure 9: Brightness temperature maps T_r reconstructed with the ill-posed approach (a) and with the regularized one (b). Here, the complex visibilities V were blurred by adding a Gaussian noise ΔV with standard deviation $\sigma_{\Delta V}$ equal to 0.08 K on both the real and imaginary parts. These maps are to be compared to the brightness temperature map T_w shown in Figure 6b. The minumum norm solution $T_r = \mathbf{G}^+V$ (a) is here obtained through the computation of the More-Penrose pseudo-inverse $\mathbf{G}^+ = \mathbf{G}^*(\mathbf{G}\mathbf{G}^*)^{-1}$, while the band-limited solution $T_r = \mathbf{U}^*\mathbf{Z}\mathbf{A}^+V$ (b) is obtained through the computation of the resolving matrix $\mathbf{A}^+ = (\mathbf{A}^*\mathbf{A})^{-1}\mathbf{A}^*$. Some differences between the two reconstructions can be observed: the rms error $\sigma_{\Delta T}$ between T_w and $T_r = \mathbf{G}^+V$ is here about 2.118 K, while it is of the order of 0.938 K between T_w and $T_r = \mathbf{U}^*\mathbf{Z}\mathbf{A}^+V$.

To investigate further on the propagation of the input errors ΔV from V to T_r through the two reconstruction operators $\mathbf{G}^+$ and $\mathbf{U}^*\mathbf{Z}\mathbf{A}^+$, simulations have been performed with $\sigma_{\Delta V}$ in the range $[0, 0.2]$ K. Shown in Figure 10 are the results of 10000 random trials of $\|\Delta V\|_F$ and their counterparts $\|\Delta T_r\|_E$. The situation is better than that governed by inequalities (20) and (25): in both cases the actual error amplification factor is smaller than the condition numbers of $\mathbf{G}$ and $\mathbf{A}$. Indeed, it turns out that $\mathcal{C}(\mathbf{G}) = 170$ and $\mathcal{C}(\mathbf{A}) = 2$, while the averaged amplification factors of errors shown in Figure 10 are only of the order of 30 and 0.66, respectively.

Remark. Keeping in mind that the relation between T_r and V, and therefore between ΔT_r and ΔV, is not a Fourier transform, it is not surprising to found an averaged amplification

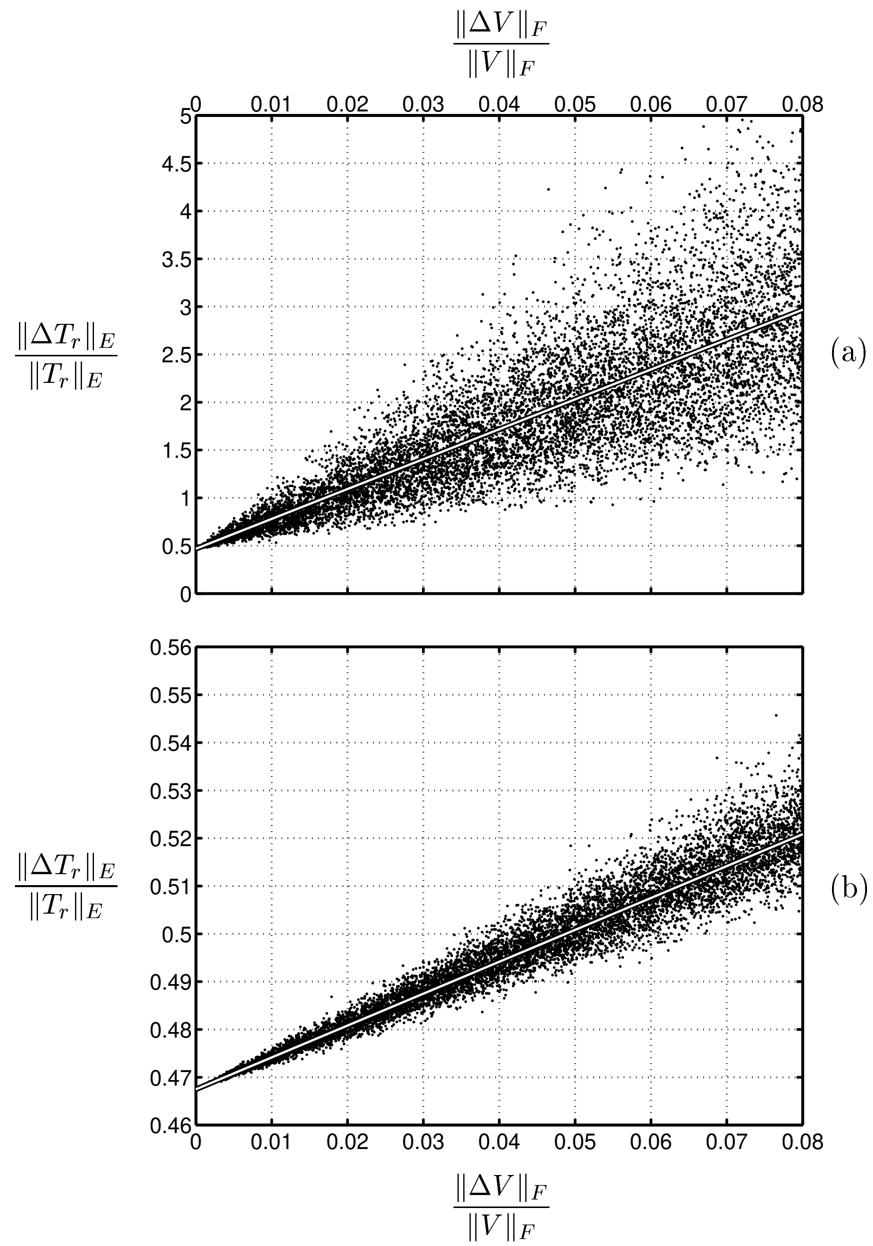

Figure 10: Propagation of input errors through the reconstruction process (the ratios are here expressed in percent): minimum norm solution $T_r = \mathbf{G}^+V$ (a) and band-limited one $T_r = \mathbf{U}^*\mathbf{Z}\mathbf{A}^+V$ (b). The noise ΔV added to the complex visibilities V is a Gaussian one with standard deviation $\sigma_{\Delta V}$ on both the real and imaginary parts: each dot represents one random trial out of 10000 with $\sigma_{\Delta V}$ in the range $[0, 0.2]$ K. The slope of the white lines represents the averaged amplification factor of errors. Here they are of the order of 30 for the ill-posed approach and 0.66 for the regularized one, while the condition numbers of the corresponding matrices $\mathbf{G}$ and $\mathbf{A}$ are equal to 170 and 2, respectively. This is the proof of the stability of the solution provided by the regularized approach.

factor of errors less than one, since the Parseval theorem could not be applied in this case, and also because the action of the regularized reconstruction operator is that of a projector.

This different behavior with respect to the propagation of errors between the two methods is not surprising since the first approach attempts to solve an ill-posed problem, while the second second one solves a regularized one. The behavior of the first approach can be summarized by the words of Fischman *et al.* [25]: "Although $\mathbf{G}^+$ reconstruction yields the desired signal response, noise in the image will inevitably increase through this method." This is not the case of the $\mathbf{U}^*\mathbf{Z}\mathbf{A}^+$ reconstruction for which the propagation of errors is under control. This behavior is emphasized by the singular values spectrum of the matrices $\mathbf{G}$ and $\mathbf{A}$. Indeed, the smallest singular values of $\mathbf{G}$ shown in Figure 11a play an important role in the pseudo-inversion of $\mathbf{G}$ and are responsible for the large amplification factor illustrated in Figure 10a. This is not the case of the singular values of $\mathbf{A}$ shown in Figure 11b.

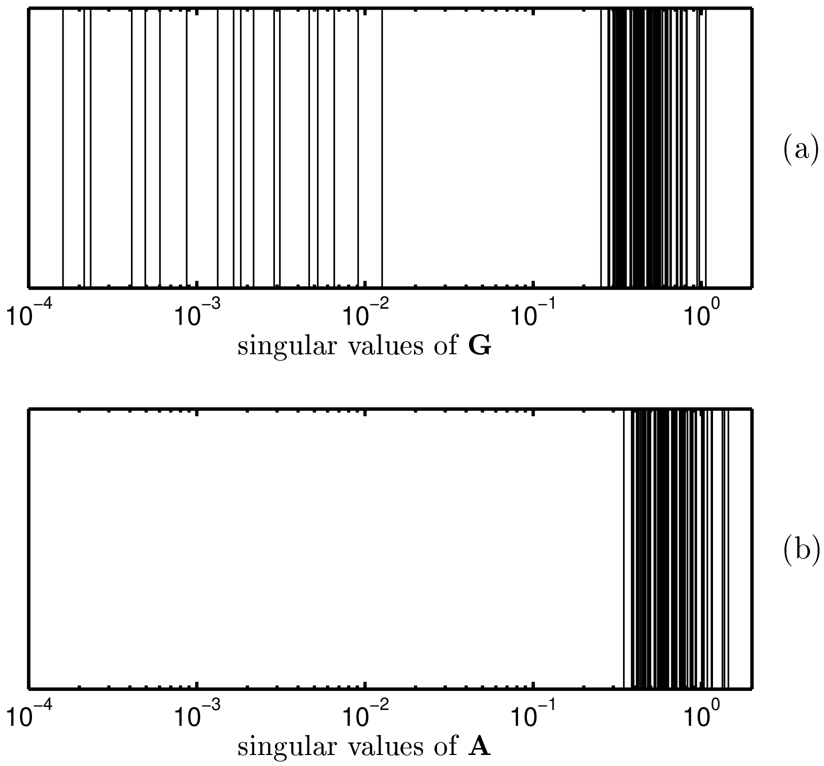

Figure 11: Singular values of the rectangular matrices $\mathbf{G}$ (a) and $\mathbf{A}$ (b). Both matrices are of full-rank and therefore have singular values greater than 0. However, it is to be noted that the 73 singular values of $\mathbf{A}$ are grouped around 1. This is not the case for the 91 singular values of $\mathbf{G}$: 73 are also confined around 1 but the 18 smallest vary on two decades with smaller values from 10^{-2} down to 10^{-4}.

This particular distribution of singular values is often encountered in many inverse problems in image processing (chap. 9 in [17]). It suggests to compute $\mathbf{G}^+$ with the aid of a TSVD (chap. 3 and 5 in [21]), rather than with the well-known expression $\mathbf{G}^*(\mathbf{G}\mathbf{G}^*)^{-1}$, so that the smallest singular values are discarded prior to inversion.

This kind of approach could be termed "numerical regularization," as opposed to the "physical regularization" performed in section 4.3, but should however lead to similar results. To verify this assertion, brightness temperature maps $T_r = \mathbf{G}^+ V$ have been reconstructed from the same blurred visibilities as those used in Fig 9a, but here $\mathbf{G}^+$ has been computed with the aid of a TSVD in which only the 73 largest singular values of $\mathbf{G}$ were retained. As expected, the results are very close to those obtained with the regularized approach shown in Figure 9b: now $\mathcal{C}(\mathbf{G})$ is equal to 2 and the averaged amplification factor of errors is about 0.66, that is to say 0.54 K/K, while the systematic error is still 1.010 K.

Remark. A useful analytic formulation based on the assumption of a reconstruction with a simple inverse Fourier transform is given by relation (15) in [24]. However, in this approach the standard deviation of the ouput error is computed with respect to the "modified brightness temperature" maps $\widetilde{T}_w$ and $\widetilde{T}_r$ rather than between T_w and T_r. In such a case, it turns out that the amount of the rms error $\sigma_{\Delta \widetilde{T}}$ which is attributable to the propagation of ΔV through a regularized reconstruction process is now about 0.25 K for $\sigma_{\Delta V} = 0.08$ K. The averaged amplification factor is therefore close to 3.13 K/K. This value is in agreement with the value provided by relation (15) in [24] which gives 3.08 K/K under the same numerical conditions.

The choice of the apodization function can be subject to discutions. However, as argued at the end of section 4.3, the effect of the window does not change the relative performances of one approach as compared to another one. More precisely, as illustrated in Table 3, the propagation of radiometric input errors is exactly the same for the regularized reconstruction operators $\mathbf{G}^+$ and $\mathbf{U}^*\mathbf{Z}\mathbf{A}^+$, while the systematic error is always slightly less for the latter one. It can be observed that the smoother is the window, the smaller are these errors. Recall that the Y-shaped array used for these simulations is equipped with only 3 antennae per arm; the values given in this table, which of course depend on the resolution level of the instrument, are thus not representative of performances expected for the SMOS instrument.
The choice of the input errors added to the complex visibilities can also be subject to discussions. However, the aim of the simulations presented here is not to make a detailed review of the errors that may affect SAIR. Their purpose is simply to illustrate this propagation, and to verify the good stability of the regularized resolving matrix reconstruction procedure for a real instrument with non identical subsystems with regard to the simple Fourier reconstruction for an ideal one. We have shown that it is possible to reach the same goal, provided that the reconstruction process is regularized and takes into account the imperfections of the subsystems of the real interferometer. This analysis has of course to be investigated further on. In particular, the propagation of modelling errors has to be inspected. This detailed study will be presented in a forthcoming working note.

6 Conclusions

The retrieval of the radiometric brightness temperature distribution from complex visibility samples provided by a synthetic aperture imaging radiometer (SAIR) has been addressed. It has been proved that this kind of problem does not have a unique and sta-

Table 3: Effect of the apodization window on the propagation of errors.

	$\sigma^{\,0}_{\Delta T}$		$\dfrac{\sqrt{(\sigma_{\Delta T})^2 - (\sigma^{\,0}_{\Delta T})^2}}{\sigma_{\Delta V}}$
window	$\mathbf{G}^+$	$\mathbf{A}^+$	$\mathbf{G}^+$ and $\mathbf{A}^+$
Rectangle	3.52 K	3.36 K	1.25 K/K
Bartlett	1.16 K	1.08 K	0.53 K/K
Welch	1.86 K	1.73 K	0.78 K/K
Connes	1.17 K	1.09 K	0.58 K/K
Parzen	0.45 K	0.43 K	0.35 K/K
Lanczos	1.45 K	1.35 K	0.66 K/K
Papoulis	0.58 K	0.55 K	0.39 K/K
Cosine	1.70 K	1.58 K	0.74 K/K
Hanning	1.01 K	0.94 K	0.54 K/K
Hamming	1.18 K	1.10 K	0.58 K/K
Blackman	0.66 K	0.62 K	0.42 K/K
Nutall	0.65 K	0.61 K	0.42 K/K
Harris	0.39 K	0.38 K	0.33 K/K

ble solution. It has been verified that the discretization of such an ill-posed problem leads to an algebraic linear system that is ill-conditioned. Consequently, the noise affecting the experimental visibilities may be transferred to a reconstructed brightness temperature map with a large amplification factor.

The approach presented in this working note intends to cure the ill-posedness of the problem. Since SAIR instruments are band-limited imaging devices, the problem has been reformulated by taking into account the capabilities of these instruments. More precisely, the regularization method adopted here consists in forcing the retrieved brightness temperature map to comply with an additional constraint derived from the physics of the problem. This family of regularization methods is now one of the most powerful tools for solving ill-posed inverse problems, another one being provided by the Bayesien methods where the additional information used is of statistical nature.

The problem to be solved has been stated and analyzed without any reference to a particular numerical algorithm, and its dimension has been reduced to the minimum number of unknowns, while taking into account, in the least squares sense, all the available information, without averaging the potentially redundant one. From the numerical analysis point of view, the stability of the solution and the propagation of errors are under control. Finally, the solution can be obtained either with the aid of an iterative method, or with a direct one, the latter being well suited to real-time processing within an automatic pipeline of a ground segment. Based on preliminary results obtained for an array equipped with 24 antennae along each arm of a Y-shaped interferometer, it is estimated that this method can be put into a shape which will meet the real time requirements for the processing of SMOS telemetry data.

Appendix A

In this appendix we establish the expression of the fringe wash function for the rectangular filters defined in section 2.2. According to equations (7) and (8) we have:

$$\begin{aligned}
\widetilde{r}_{kl}(t) &\equiv \frac{1}{\sqrt{B_k B_l}} \int_{-\infty}^{+\infty} H_k(f-f_o)\overline{H}_l(f-f_o)\, \mathrm{e}^{+2\mathrm{j}\pi f t}\, \mathrm{d}f \\
&= \mathrm{e}^{\mathrm{j}(\varphi_l-\varphi_k)}\, \mathrm{e}^{2\mathrm{j}\pi(\tau_l-\tau_k)f_o}\, \mathrm{e}^{2\mathrm{j}\pi(\tau_k\bar{f}_k-\tau_l\bar{f}_l)}\, \frac{1}{\sqrt{B_k B_l}} \int_{f_m}^{f_M} \mathrm{e}^{2\mathrm{j}\pi(\tau_l-\tau_k+t)f}\, \mathrm{d}f \\
&= \mathrm{e}^{\mathrm{j}(\varphi_l-\varphi_k)}\, \mathrm{e}^{2\mathrm{j}\pi(\tau_l-\tau_k)f_o}\, \mathrm{e}^{2\mathrm{j}\pi(\tau_k\bar{f}_k-\tau_l\bar{f}_l)}\, \mathrm{e}^{\mathrm{j}\pi(\tau_l-\tau_k+t)(f_M+f_m)} \\
&\qquad \times \frac{f_M-f_m}{\sqrt{B_k B_l}}\, \mathrm{sinc}\big((\tau_l-\tau_k+t)(f_M-f_m)\big)
\end{aligned}$$

where:

$$\begin{aligned}
f_m &= \max(-B_k/2+\bar{f}_k, -B_l/2+\bar{f}_l) - f_o \\
f_M &= \min(+B_k/2+\bar{f}_k, +B_l/2+\bar{f}_l) - f_o
\end{aligned}$$

are the extrem frequencies of the overlapping regions of the two filters. It is easy to check that for receivers equipped with identical band-pass filters centred on $\bar{f} = f_o$, this expression reduces to $\mathrm{sinc}(Bt)$ since in this case $f_m = -B/2$ and $f_M = +B/2$.

Appendix B

In this appendix we establish the definition of the adjoint of the modelling operator $\mathbf{G}$. According to the definition of $\mathbf{G}$ in (19) and to those of the inner products in E and F:

$$\begin{aligned}
(T^{(1)} \mid T^{(2)})_E &= \sigma_{\boldsymbol{\xi}} \sum_{\mathbf{p}\in\mathbb{G}(\mathcal{H}^*)} \overline{T}^{(1)}_{\mathbf{p}}\, T^{(2)}_{\mathbf{p}} \\
(V^{(1)} \mid V^{(2)})_F &= \sigma_{\mathbf{u}} \sum_{k,l=1}^{\ell} \overline{V}^{(1)}_{kl}\, V^{(2)}_{kl}
\end{aligned}$$

we have:

$$\begin{aligned}
(V \mid \mathbf{G}T)_F &\equiv \sigma_{\mathbf{u}} \sum_{k,l=1}^{\ell} \overline{V}_{kl} (\mathbf{G}T)_{kl} \\
&= \sigma_{\mathbf{u}} \sum_{k,l=1}^{\ell} \overline{V}_{kl}\, \sigma_{\boldsymbol{\xi}} \sum_{\mathbf{p}\in\mathbb{G}(\mathcal{H}^*)} \frac{F_{k,\mathbf{p}}\, \overline{F}_{l,\mathbf{p}}\, T_{\mathbf{p}}}{\sqrt{1-\|\boldsymbol{\xi}_{\mathbf{p}}\|^2}}\, \widetilde{r}_{kl}\Big(\frac{-\mathbf{u}_{kl}\boldsymbol{\xi}_{\mathbf{p}}}{f_o}\Big)\, \mathrm{e}^{-2\mathrm{j}\pi\mathbf{u}_{kl}\boldsymbol{\xi}_{\mathbf{p}}} \\
&= \sigma_{\boldsymbol{\xi}} \sum_{\mathbf{p}\in\mathbb{G}(\mathcal{H}^*)} T_{\mathbf{p}}\, \sigma_{\mathbf{u}} \sum_{k,l=1}^{\ell} \frac{F_{k,\mathbf{p}}\, \overline{F}_{l,\mathbf{p}}\, \overline{V}_{kl}}{\sqrt{1-\|\boldsymbol{\xi}_{\mathbf{p}}\|^2}}\, \widetilde{r}_{kl}\Big(\frac{-\mathbf{u}_{kl}\boldsymbol{\xi}_{\mathbf{p}}}{f_o}\Big)\, \mathrm{e}^{-2\mathrm{j}\pi\mathbf{u}_{kl}\boldsymbol{\xi}_{\mathbf{p}}} \\
&= \sigma_{\boldsymbol{\xi}} \sum_{\mathbf{p}\in\mathbb{G}(\mathcal{H}^*)} \overline{(\mathbf{G}^*V)}_{\mathbf{p}}\, T_{\mathbf{p}} \;\equiv\; (\mathbf{G}^*V \mid T)_E
\end{aligned}$$

hence the definition of $\mathbf{G}^*$:

$$\begin{array}{rcl} \mathbf{G}^* : F & \longrightarrow & E \\ V & \longmapsto & \mathbf{G}^* V = T \end{array}$$

with, for any $\mathbf{p}$ in $\mathbb{G}(\mathcal{H}^*)$:

$$T_{\mathbf{p}} = \sigma_{\mathbf{u}} \sum_{k,l=1}^{\ell} \frac{\overline{F}_{k,\mathbf{p}}\, F_{l,\mathbf{p}}}{\sqrt{1 - \|\boldsymbol{\xi}_{\mathbf{p}}\|^2}}\, V_{kl}\, \overline{\widetilde{r}}_{kl}\Big(\frac{-\mathbf{u}_{kl}\boldsymbol{\xi}_{\mathbf{p}}}{f_o}\Big)\, \mathrm{e}^{+2\mathrm{j}\pi \mathbf{u}_{kl}\boldsymbol{\xi}_{\mathbf{p}}}.$$

Acknowledgments

This work was supported by CNES, CNRS and the Région Midi-Pyrénées (under the grant 99009020), data processing support was provided by CERFACS. The European Space Agency (ESA) is leading the SMOS project. The author is very grateful to Philippe Waldteufel from IPSL and Yann Kerr from CESBIO for fruitful discussions and instructive comments throughout this work. The author also acknowledges Serge Gratton from CERFACS for his help in the formulation of the optimization problem to be solved, and Ph.D. student Bruno Picard from CERFACS for his contributions to the numerical simulations.

References

[1] Y.H. Kerr, P. Waldteufel, J.-P. Wigneron, J.-M. Martinuzzi, J. Font, and M. Berger, *Soil Moisture Retrieval from Space: The Soil Moisture and Ocean Salinity (SMOS) Mission*, IEEE Transactions on Geoscience and Remote Sensing, 39(**8**), pp. 1729-1735, 2001.

[2] M. Martin-Neira, Y. Menard, J.-M. Goutoule and U. Kraft, *MIRAS, a two-dimensional aperture synthesis radiometer*, Proc. of IGARSS'94 (Pasadena, California, USA), pp. 1323-1325, 1994.

[3] A.R. Thompson, G.W. Swenson and J.W. Moran, *Interferometry and Synthesis in Radio Astronomy*, John Wiley & Sons Inc., 1st ed., 1986.

[4] U.R. Kraft, *Spaceborne synthetic aperture interferometric radiometers for global monitoring of the Earth*, Proc. of IGARSS'91 (Helsinky, Finland), pp. 971-974, 1992.

[5] A. Camps, J. Bara, I. Corbella, and F. Torres, *The Processing of Hexagonally Sampled Signals with Standard Rectangular Techniques: Application to 2D Large Aperture Synthesis Interferometric Radiometers*, IEEE Transactions on Geoscience and Remote Sensing, 35(**1**), pp. 183-190, 1997.

[6] F.T. Ulaby, R.K. Moore and A.K. Fung, *Microwave Remote Sensing, Active and Passive: Fundamentals and Radiometry (Vol. 1)*, Artech House Inc., 1st Edition (456 pp), 1981.

[7] C.S. Ruf, C.T. Swift, A.B. Tanner, and D.M. LeVine, *Interferometric synthetic aperture radiometry for the remote sensing of the Earth*, IEEE Transactions on Geoscience and Remote Sensing, 26(**5**), pp. 597-611, 1988.

[8] F. Bayle, J.-P. Wigneron, Y.H. Kerr, P. Waldteufel, E. Anterrieu, J.-C. Orlhac, A. Chanzy, O. Marloie, M. Bernardini, S. Sobjaerg, J.-C. Calvet, J.-M. Goutoule, and N. Skou, *Two-dimensional synthetic aperture images over a land surface scene*, IEEE Transactions on Geoscience and Remote Sensing, 40(**3**), pp. 710-714, 2002.

[9] A. Camps, *Application of interferometric radiometry to Earth observation*, Ph.D. Thesis, Universitat Politecnica de Catalunya (Barcelona, Spain), 1996.

[10] A. Camps, J. Bara, F. Torres, I. Corbella and J. Romeu, *Impact of antenna errors on the radiometric accuracy of large aperture synthesis radiometers*, Radio Science, 32(**2**), pp. 629-641, 1997.

[11] F. Torres, A. Camps, J. Bara, and I. Corbella, *Impact of receiver errors on the radiometric resolution of large two-dimensional aperture synthesis radiometers*, Radio Science, 32(**2**), pp. 657-668, 1997.

[12] A. Lannes, E. Anterrieu, and K. Bouyoucef, *Fourier Interpolation and Reconstruction via Shannon-type Techniques; Part I: regularization principle*, Journal of Modern Optics, 41(**8**), 1537-1574, 1994.

[13] A. Lannes, E. Anterrieu, and K. Bouyoucef, *Fourier Interpolation and Reconstruction via Shannon-type Techniques Part II: technical developments and applications*, Journal of Modern Optics, 43(**1**), pp. 105-138, 1996.

[14] E. Anterrieu, P. Waldteufel, and A. Lannes, *Apodization functions for 2D hexagonally sampled synthetic aperture imaging radiometers*, IEEE Transactions on Geoscience and Remote Sensing, 40(**12**), pp. 2531-2542, 2002.

[15] R.M. Mersereau, *The processing of hexagonally sampled two-dimensional signals*, Proc. IEEE, 67(**6**), pp. 930-949, 1979.

[16] S. Twomey, *Introduction to the Mathematics of Inversion in Remote Sensing and Indirect Measurements*, Elsevier Science, 1st ed., 1977.

[17] M. Bertero and P. Boccacci, *Introduction to Inverse Problems in Imaging*, Institute of Physics Publishing, 1st ed., 1998.

[18] G.H. Golub and C.F. Van Loan, *Matrix Computations*, Johns Hopkins Univ. Press, 3rd ed., 1996.

[19] A. Camps, J. Bara, F. Torres, and I. Corbella, *Extension of the Clean technique to the microwave imaging of continuous thermal sources by means of aperture synthesis radiometers*, Progress in Electromagnetism Research, PIER 18, pp. 67-83, 1998.

[20] A.B. Tanner and C.T. Swift, *Calibration of a synthetic aperture radiometer*, IEEE Transactions on Geoscience and Remote Sensing, 31(**1**), pp. 257-267, 1993.

[21] C. Hansen, *Rank-Deficient and Discrete Ill-Posed Problems*, Society for Industrial & Applied Mathematics, 1st ed., 1998.

[22] A. Bjorck, *Numerical Methods for Least Squares Problems*, Society for Industrial & Applied Mathematics, 1st ed., 1996.

[23] J. Bara, A. Camps, F. Torres, and I. Corbella, *Angular resolution of two-dimensional hexagonally sampled interferometric radiometers*, Radio Science, 33(**5**), pp. 1459-1473, 1998.

[24] A. Camps, I. Corbella, J. Bara, and F. Torres, *Radiometric sensitivity computation in aperture synthesis interferometric radiometry*, IEEE Transactions on Geoscience and Remote Sensing, 36(**2**), pp. 680-685, 1998.

[25] M.A. Fischman, A.W. England, and C.S. Ruf, *How digital correlation affects the fringe washing function in L-band aperture synthesis radiometry*, IEEE Transactions on Geoscience and Remote Sensing, 40(**3**), pp. 671-679, 2002.